1

Enhanced methanol electro-oxidation activity of nanoclustered gold

3

Anupam Yadav,* Yejun Li, Ting-Wei Liao, Kuo-Juei Hu, Jeroen E. Scheerder, Olga V.
Safonova, Tibor Höltzl, Ewald Janssens, Didier Grandjean,* and Peter Lievens*

Anupam Yadav, Dr. Ting-Wei Liao, Dr. Kuo-Juei Hu, Dr. Jeroen E. Scheerder, Prof. Ewald Janssens,
Dr. Didier Grandjean, Prof. Peter Lievens
Quantum Solid-State Physics, Department of Physics and Astronomy, KU Leuven, Celestijnenlaan
200D, Leuven 3001, Belgium

Dr. Yejun Li
Hunan Key Laboratory of Super Microstructure and Ultrafast Process, School of Physics and
Electronics, Central South University, Changsha, Hunan 410083, China

Dr. Olga V. Safonova
Paul Scherrer Institute, Villigen PSI 5232, Switzerland

Dr. Tibor Höltzl
Furukawa Electric Institute of Technology, Budapest 1158, Hungary
and
MTA-BME Computation Driven Chemistry Research Group and Department of Inorganic and
Analytical Chemistry, Budapest University of Technology and Economics, Budapest 1111, Hungary

E-mail: anupam.yadav@kuleuven.be, didier.grandjean@kuleuven.be, peter.lievens@kuleuven.be

Abstract

Size-selected 3 nm gas phase Au clusters dispersed by cluster beam deposition on a conducting

fluorine-doped tin oxide template show strong enhancement in mass activity for the methanol

electro-oxidation reaction compared to previously reported nanostructured gold electrodes.

Density functional theory based modelling on the corresponding Au clusters guided by

experiments attributes this high methanol electro-oxidation activity to the high density of

exposed under-coordinated Au atoms at their faceted surface. In the description of the activity

trends, vertices and edges are the most active sites due to their favorable CO and OH adsorption

energies. The faceted structures occurring in this size range, partly preserved upon deposition,

may also prevent destructive restructuring during the oxidation-reduction cycle. These results

45 highlight the benefits of using cluster beam deposition in fine-tuning material properties on the

46 nanoscale and designing high-performance fuel cell electrodes with less material usage.

47
48
49
50 **Introduction**
51
52 Direct Methanol Fuel Cell (DMFC)[1] is a rapidly emerging clean energy technology that

53 enables the direct conversion of the chemical energy stored in methanol fuel to electricity.[2]

54 However, its widespread commercialization is currently hindered by an extensive usage of

55 precious noble metals as catalyst in order to drive high methanol consumption and energy

56 conversion efficiency. Therefore, reducing their usage yet maintaining favorable

57 electrochemical activities becomes necessary for any practical energy harvesting application of

58 DMFCs.[3]

59 Another challenge is to maintain good catalyst stability at low loadings under DMFC operating

60 conditions.[4] For example, Pt is strongly poisoned by the accumulation of the methanol electro-

61 oxidation (MEO) reaction residues such as COH and CO on its surface, compromising the

62 device durability.[5] Switching from an acid electrolyte to an alkaline one and/or making

63 combinations with oxophilic components enhances Pt activity, given that the presence of

64 adsorbed OH accelerates the CO oxidation step.[6] However, such aqueous conditions corrode

65 Pt considerably over time and potentially deteriorate its overall performance.[7, 8]

66 Developing a non-Pt electrocatalyst based on Au that features good activity, tolerance to

67 intermediate carbon residue poisoning, and stability under alkaline conditions is also a

68 promising strategy.[9, 10, 11] However, the inefficient kinetics of bulk Au MEO catalysts hinders

69 their practical applications in DMFCs.[12-14] In contrast, gold nanoparticles (NPs) supported on

70 polyaniline (PANI)[15] and activated carbon (Au/C) have demonstrated a remarkable activity in

71 MEO reaction, [10, 16] as well as in reduction of carbon dioxide and oxygen evolution reaction

72 (OER).[17, 18] Poorly active in its bulk form, Au in the form of NPs and clusters below 6 nm in

73 diameter exhibit indeed an extraordinary high catalytic activity for numerous oxidation and

74 reduction (electro)catalytic reactions.[19, 20, 21] CO oxidation reaction over TiO_2 supported Au

75 clusters was found to be highly dependent on size of the Au clusters with a maximum activity

76 occurring at 3.2 nm.[22] Similar size effects have been demonstrated for Au NPs used as

77 electrocatalyst for the oxygen reduction reaction (ORR), where the activity also reaches a

78 maximum for a particle size around 3 nm.[23, 24]

79 Among the numerous effects at the origin of the unusual catalytic properties of nanosized Au

80 such as the preparation method and activation procedure, the Au layer thickness, the interaction

81 with the support material and the intrinsic cluster strain, the availability of many under-

82 coordinated Au atoms on the small particles is by far the dominant one.[19, 25] Most of the surface

83 Au atoms in small particles are likely to participate in chemisorption of the reactants, the

84 propensity of which depends on the extent of coordination of the Au atom(s) acting as

85 adsorption site.[26] Both O and CO binding energies are lowered (stronger bonding) by up to ca.

86 1 eV going from 9-fold coordinated Au atoms on Au(111) faces to 4-fold coordinated Au atoms

87 in Au_{10} clusters.[19] This directly results from an upshift towards the Fermi level of the d states

88 of the low coordinated Au atoms enabling strong interaction of those d states with the O 2p

89 valence states.[19, 27]

90 Designing higher performance Au catalysts requires increasing the concentration of under-

91 coordinated sites of relatively low coordination number at the surface of gold. This could be

92 achieved by decreasing the Au particle size,[19] but also by controlling the particle shape and

93 crystalline structure.[28] Conventional chemical preparation methods have demonstrated only

94 modest abilities to control the structural properties of Au NPs. Highly dispersed Au catalysts

95 prepared by dc sputtering, deposition-precipitation, gas-phase, and liquid-phase grafting of

96 organo-gold complexes using an Al_2O_3, SiO_2, or TiO_2 support with relative control over Au

97 NPs mean diameter and shape exhibit higher overall catalytic activities compared with those

98 prepared by impregnation.[29] Although preformed size-selected Au colloids allow for a better

99 definition of the particle size, the presence of protecting ligands is generally limiting their

100 catalytic activity and preventing the formation of a crystalline faceted surface.[30] Moreover,

101 removal of the ligands to obtain catalytically active "naked particles" requires additional,

102 possibly destructive, activation treatments.[21] Direct electrodeposition of large Au NPs on the

103 electrode surface[15] was also reported but only limited size selection was obtained.

104 Cluster beam deposition (CBD) combined with mass selection is a physical method that allows

105 production of naked Au clusters highly controlled in terms of particle size, deposition energy,

106 and coverage (average density) on any type of substrate surface.[31, 32] Such Au clusters as

107 produced and deposited by CBD are free of surfactant molecules and generally possess well-

108 defined atomic configurations specific to the cluster size and that can differ significantly from

109 the bulk,[32] as demonstrated for size-selected Au_{20},[33] Au_{55},[34] Au_{309},[35] and Au_{923}[36]. Besides,

110 CBD synthesis can be adjusted in a way that most of these clusters possess highly faceted

111 structures with a high concentration of edge and vertex surface atom sites and a limited fraction

112 of amorphous structures (below 22% in a study of Au_{923}).[32] The use of these well-defined Au

113 clusters, produced in the gas phase and beam-deposited subsequently, as catalysts may

114 contribute to obtaining a clear understanding of nanocatalysis at atomic or molecular scale that

115 still remains elusive.[30, 37] In the remainder of this paper we refer to these clusters as NC. NC

116 stands for nanoclusters, where nano refers to the size of the particles and cluster refers to the

117 gas phase cluster beam production methodology used.

118 In this paper, we describe a highly active DMFC anode for the MEO reaction based on dispersed

119 3 nm diameter Au NCs, corresponding to the optimal activity size reported for (electro)catalytic

120 reactions. We demonstrate that CBD synthesis of size-selected Au clusters offers efficient and

121 stable utilization of active metal.[23] [38] The structural and electrochemical properties of

122 deposited Au NCs were evaluated by a combination of aberration-corrected Scanning

123 Transmission Electron Microscopy (STEM) employing High Angle Annular Dark Field

124 (HAADF) detectors, X-ray Absorption Fine Structure (XAFS) spectroscopy, Scanning Electron

125   Microscopy (SEM) and Cyclic Voltammetry (CV) techniques. Au NCs on fluorine-doped tin

126   oxide (FTO) demonstrate a strongly enhanced MEO activity in comparison to Au colloids

127   synthesized by wet chemistry and drop-casted on FTO supports. The intrinsic activity of the

128   naked Au cluster is rationalized using Density Functional Theory (DFT). Calculations based on

129   model clusters of this size allow achieving a comprehensive understanding of the role of

130   different Au NCs surface sites in the MEO process.

131

132   **Main Text**

133   A home built magnetron sputtering CBD setup was used for producing Au clusters. Following

134   deposition their structural properties were characterized in detail by various methods (**Figure**

135   **1**). In brief, Au clusters were synthesized by condensation of Ar sputtered Au atoms from a

136   bulk Au target in a controlled atmosphere of Ar and He, while the condensation chamber was

137   cooled to liquid nitrogen temperatures. Preformed cationic Au clusters were size-filtered during

138   flight using an orthogonal ion bender and subsequently deposited on either carbon TEM grids,

139   boron doped amorphous SiO_2/Si (100) wafers, or FTO supports held at room temperature under

140   UHV conditions. Precise tuning of the deposition energy and the particle density on the surface

141   was achieved by adjusting the substrate bias voltage, ensuring soft landing of isolated clusters

142   with a kinetic energy of less than 0.2 eV per atom, and monitoring the current from the beam

143   of charged clusters, respectively. The surface coverage was kept below 20% of a monolayer of

144   size-selected Au NCs. As will be discussed further on, under these conditions cluster

145   fragmentation and agglomeration is limited. Unlike wet chemistry, no further calcination or

146   activation steps are required after deposition.

a)

b)

c)

Clusters Focusing

Clusters Size Selection

Magnetron Clusters Source

d)

e)
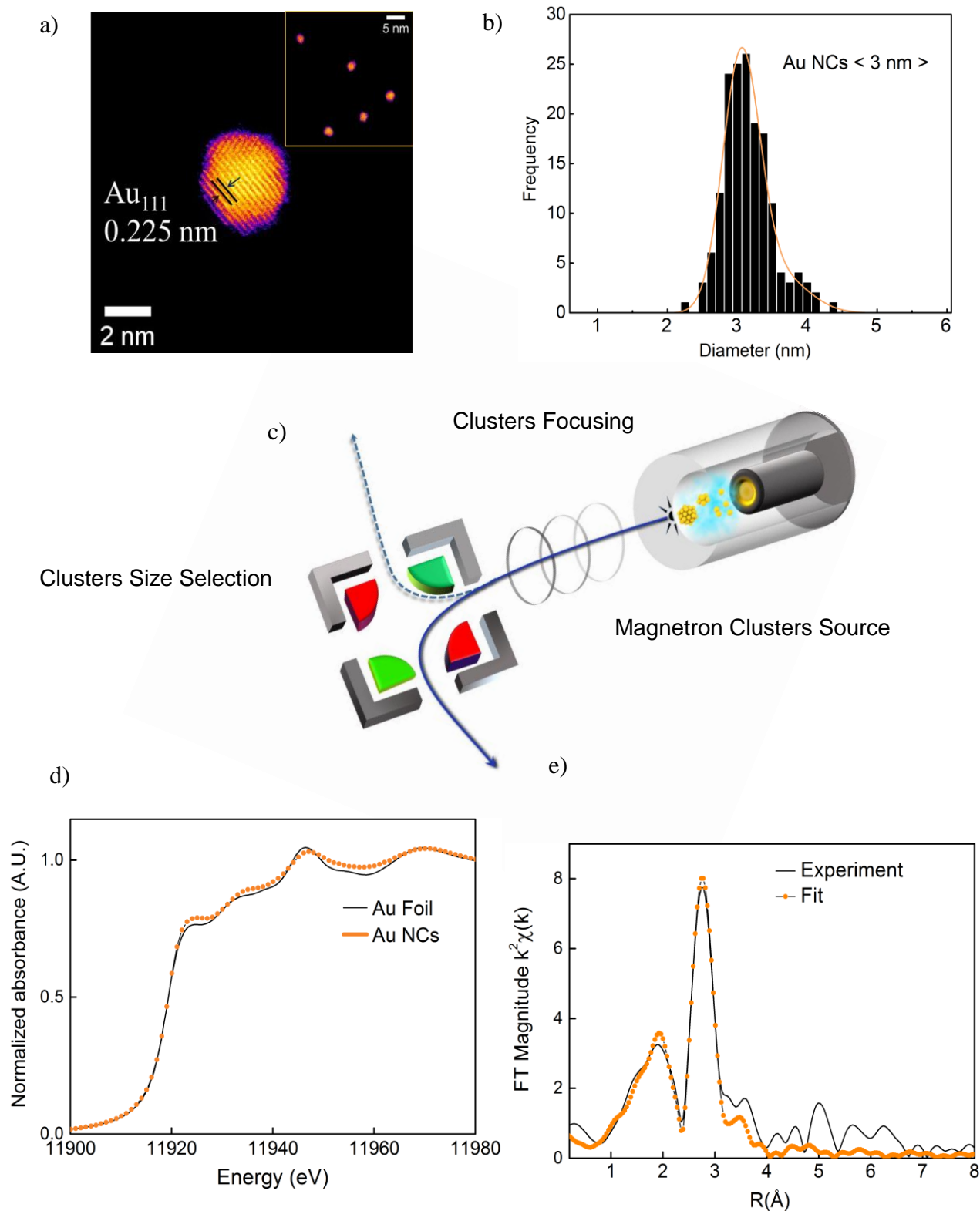
Figure 1: Synthesis and atomic scale structural properties of Au NCs. (a) Sub-Ångström resolution STEM-HAADF images of Au NCs. (b) Histogram distribution of Au NCs diameter. (c) Schematic illustration of magnetron CBD technology. (d) Fluorescence detected Au L_3 XANES of Au NCs on a $SiO_2/Si(100)$ wafer compared to a reference Au foil. (e) Best fit of Au NCs Fourier transform of k^2 weighted EXAFS.

148   A representative STEM-HAADF image of a surfactant-free Au NC with sub-Ångström

149   resolution is presented together with the histogram of Au NCs size distribution in Figures 1a

150   and 1b, respectively. The STEM image shows that the preformed Au clusters remain intact

151   upon deposition, presenting a sharp narrow particle size distribution on the surface. A mean

152   diameter of Au NCs of 3.0 nm with a standard deviation of 0.3 nm was obtained by measuring

153   over 160 NCs. The shoulder in the distribution at 4 nm corresponds to a fraction of about 10%

154   of doubly charged clusters of twice the mass of the main peak in the distribution that are selected

155   together with the singly charged smaller clusters by the quadrupole bender. Detailed STEM

156   analysis indicates that individual Au NCs have ordered faceted geometries, with identifiable

157   lattice fringes matching the Au(111) atomic plane configuration (Figure 1a and S1). This is in

158   line with an earlier study of well-defined Au_{923} prepared by CBD, whose population is

159   composed of a mixture of icosahedral (Ih), decahedral (Dh), and face-centered cubic (FCC)

160   structural motifs.[32] The individual fractions of aforementioned structures depend on the

161   synthesis parameters.[32]

162   Electron microcopy characterization was complemented by the determination of the average

163   structural and electronic properties of Au NCs deposited on a silicon wafer using XAFS

164   spectroscopy. The Au L_3-edge XANES (X-ray Absorption Near Edge Structure) of the Au NCs

165   shows damped oscillations compared to reference Au metal foil, confirming their nanosize

166   (Figure 1d). The edge position overlaps with that of Au foil confirming the absence of isolated

167   cationic Au species on the support. The modest white line intensity observed has been ascribed

168   to the completely filled d-orbitals of metallic Au.[39] The combined XANES edge position and

169   white-line intensity thereby provides direct evidence that the Au NCs are predominantly

170   composed of Au species in zero-valence state. The best fit of the Fourier transform of the k^2-

171   weighted Au L_3 edge EXAFS (Extended X-ray Absorption Fine Structure) (Figure S2) and the

172   corresponding structural results are presented in Figure 1e and Table S1, respectively. The first

173   shell coordination number (CN) is reduced to 10.3 versus 12 in a bulk Au foil, highlighting the

174   large fraction of surface atoms in the Au NCs. This value gives a theoretical diameter of (2.8 ±

175   0.8) nm fully in agreement with the STEM results.[40] The Au-Au bond distance of 2.85 Å of

176   the first coordination shell corresponds to a contraction of about 1% compared to a bulk Au foil

177   (2.88 Å), an effect that is generally observed in nanosize gold.[41] EXAFS analysis confirms

178   that the gaseous Au clusters retain their three dimensional shape upon deposition resulting from

179   soft-landing the clusters on the support and limited interaction with the surface.

180   Finally, the nanotextured surface of bare FTO (Figure S3) and that modified by Au depositions

181   was characterized by high resolution SEM. Images of FTO electrodes modified by deposition

182   of gaseous Au clusters using CBD and by colloidal Au NPs of similar size (Figure S4) prepared

183   via a wet chemistry route, used as control sample, are presented in **Figure 2**. The Au NCs,

184   identified as bright speckles, are deposited homogeneously and highly dispersed on the

185   electrode surface (Figure 2a). The global gold metal loading at the surface of the Au NCs

186   modified FTO electrode is 425 ng cm^{-2}, as determined by Rutherford Backscattering

187   Spectroscopy (RBS). It is matching the coverage estimate of 20% of a close packed monolayer

188   of Au NCs on the FTO surface derived from monitoring the NCs current during deposition.

189   Unlike Au NCs, drop-casted Au colloids were not stable against agglomeration. The sample

190   prepared from Au colloids has a metal loading of 21 µg cm^{-2}(Figure 2b).
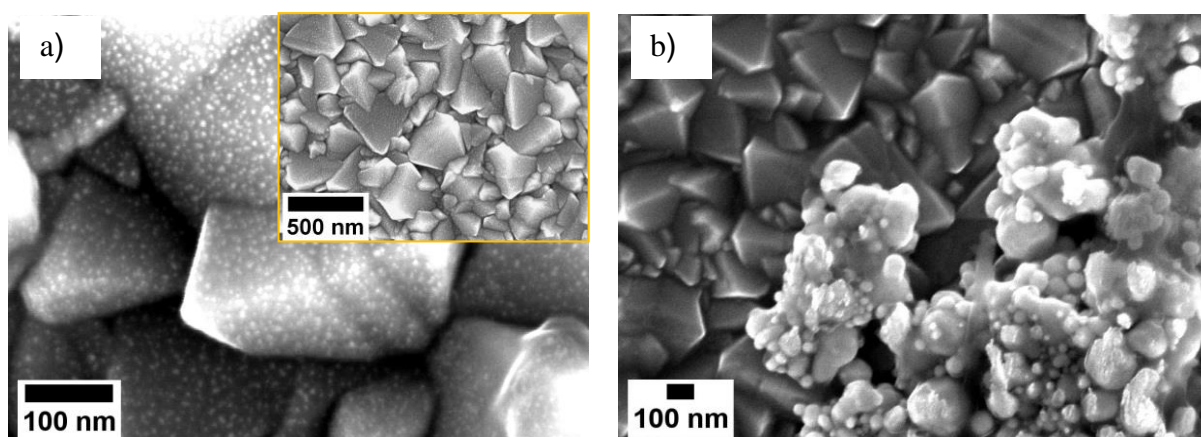
Figure 2: High Resolution SEM images of (a) Au NCs modified FTO and (b) colloidal Au modified FTO. The inset image in (a) shows the global view of deposited Au NCs.

191   The catalytic activity of the as-synthesized Au NCs modified FTO towards MEO was evaluated

192   by measuring their CV curves in a 0.5 M KOH solution at a scan rate of 20 mV s^{-1}, as shown

193   in **Figure 3**. In the methanol-free KOH solution the bare FTO electrode is inert at potentials

194   below 500 mV, in line with the requirement of minimum capacitive currents from the support
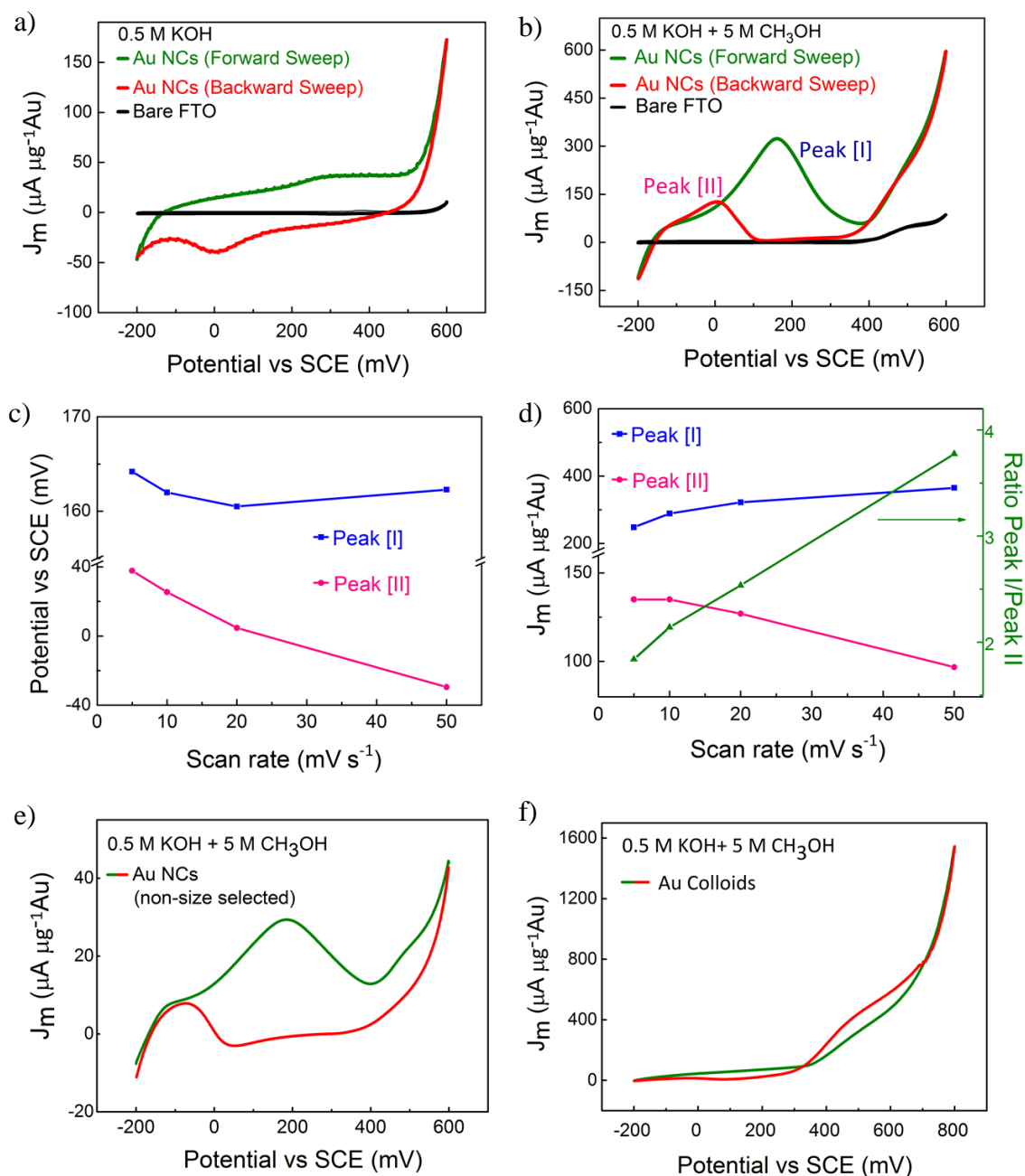
Figure 3: MEO activity of 3nm Au NCs at scanning rate of 20 mV s^{-1}. Cyclic scans of bare FTO and Au NCs modified FTO under (a) 0.5 M KOH and (b) 0.5 M KOH and 5 M CH$_3$OH. c) MEO peak potentials versus scan rate; (d) MEO peak current densities and their ratio versus scan rate. MEO activity of control Au samples (e) non size-selected gaseous Au NCs and (f) colloidal Au nanoparticles.

195   (Figure 3a). CV of Au NCs modified FTO in the methanol-free KOH solution consists of four

196   distinctive regions (Figure 3a). From 70 to 130 mV Au-OH$_{ads}^{(1-\lambda)-}$ is formed at the surface of

197   Au NCs[10, 42] according to Au + OH$^-$ → Au-OH$_{ads}$ $^{(1-\lambda)-}$ $^+$ λe-, where ads denotes chemical

198   adsorbed species on the clusters. The charge-transfer coefficient λ varies between 0 and 1.[14, 43]

199   In the second region (130-400 mV) the surface of the Au NCs is oxidized to form gold

200   (hydro)oxide species with Faradaic current flowing through the interface.[44] From 400 to 600

201   mV, a compact gold (hydro)oxide monolayer is generally formed[11] that is electrochemically

202   reduced to form a cathodic current peak at ca. 0 mV during the negative scan.[11, 14, 45] In the last

203   region around 600 mV the large current increase is likely due to the decomposition of the

204   electrolyte at high potentials resulting in the oxygen evolution reaction (OER).[46] The much

205   more limited current increase observed in the same region for bare FTO highlights the high

206   catalytic activity of Au NCs towards OER.

207   Upon addition of methanol (5M), the CV of Au NCs modified FTO in the KOH solution

208   exhibits two clear peaks related to the MEO process assigned as Peak I and II in the forward

209   and backward potential scan, respectively (Figure 3b). The low curve region of Peak I at 0.0

210   mV with an amplitude of 128 μA μg^{-1} corresponds to the onset of the oxidation of methanol

211   into formate via a four-electron transfer according to reaction (1):[14, 47] CH$_3$OH + 5OH$^-$ →

212   HCOO$^-$ + 4H$_2$O + 4e$^-$, whose intensity is limited by the low concentration of Au-OH$_{ads}^{(1-\lambda)-}$

213   formed on the gold surface atoms. As the potential increases the more concentrated Au-OH$_{ads}^{(1-}$

214   $^{\lambda)-}$ oxidize methanol into formate with enhanced efficiency forming the intense Peak I at 160

215   mV. [11, 12, 14, 47, 48] This peak that appears before the formation of a gold (hydro)oxide represents

216   an exceptional mass normalized current density of 329 μA μg^{-1} Au and an electrochemically

217   active surface area (ECSA) normalized current density of 1.85 mA cm^{-2} despite Au loading in

218   the nanogram range. The current density then decreases sharply due to the formation of a

219   (hydro)gold oxide monolayer on the surface of Au NCs that restrains the MEO by decreasing

10

220 the number of available OH_{ads}.[16] Peak I is followed, after the exchange between OH^- and O

221 species ("turnover") by an exponential burst in the current output from 400 mV onwards. It

222 corresponds to the methanol oxidation into carbonates by a compact gold (hydro)oxide

223 monolayer formed at these high potentials via a six-electron transfer reaction (2):[12, 14, 48]

224 $CH_3OH + 8OH^- \rightarrow CO_3^{2-} + 6H_2O + 6e^-$. In the backward scan, no hysteresis is observed down

225 to 400 mV suggesting that the extent of the gold (hydro)oxide formed is limited in this high

226 potential range. This is further confirmed by the absence of a electrochemical reduction peak

227 just above 0 V and the early onset of Peak II at 100 mV once the Au NC surface is free of OH_{ads}.

228 Similarly a slightly positive hysteresis is observed between 0 and -200 mV suggesting that the

229 Au NCs surfaces are not degraded compared to those observed in the first forward scan. This

230 indicates a fully reversible oxidation-reduction of the Au NC surfaces during the CV.

231 The dynamics of the methanol oxidation reaction on Au NCs estimated by adjusting the scan

232 rate (Figure S5) is summarized in Figures 3c and d. Upon increasing scan rates the potential of

233 Peak I remains constant, while Peak II shifts towards lower potentials. Peak I current increases

234 and is proportional to the square root of the scan rate, suggesting that the oxidation of methanol

235 is a Faradic process.[49] The Peak II current is higher at low scan rates, in stark contrast to the

236 typical trend seen in surface confined or diffusion controlled voltammetry.[50, 51] This is due to

237 the significant removal of OH^- by methanol from the Au NCs surface for the low scan rates.

238 This is further manifested by the shape of the CV experiment at 50 mV s^{-1} in which the

239 hysteresis builds up between the forward and backward scans above 400 mV, and the small

240 reduction peak is observed at 100 mV, causing the late onset of Peak II.

241 The MEO activity of Au NCs was compared to two similar control electrodes: i) FTO

242 supporting sub 5 nm non size-selected gaseous Au clusters prepared by an alternative laser

243 ablation CBD source (Figure S6 and 3e) and ii) FTO supporting drop-casted Au colloids

244 prepared by wet chemistry (Figure S4 and 3f). Size-selected 3 nm Au NCs show by far the best

245   electrochemical properties with a much higher activity towards MEO than both the non size-

246   selected CBD Au NCs and the chemically prepared drop-casted Au colloids.

247   Mass activity of sub 5 nm non size-selected Au NCs is 11 times lower than that of the size-

248   selected 3 nm Au NCs. Moreover a five-time increase of the non-size selected Au NCs loading

249   produces only less than a doubling of the mass activity (29 µA µg^{-1} Au to 52 µA µg^{-1} Au, Figure

250   S7). In contrast with size-selected Au NCs, the strong hysteresis between forward and backward

251   scans occurring above 400 mV indicates a marked oxidation of the NC surface that is

252   accompanied with a marked reduction peak at 0 V. At the highest scan rate of 50 mVs^{-1}, the

253   hysteresis above 400 mV is found to be more pronounced indicating stronger oxidation of the

254   Au NCs surface. Unlike low scan rates, a further drop in the Faradic current is observed below

255   -100 mV during the backward scan demonstrating that the original activity in the onset of four-

256   electron oxidation has decreased. This suggests that a substantial number of under-coordinated

257   active sites has been lost in the CV, either by an incomplete reduction and/or a restructuring of

258   the surface upon reduction highlighting the instability of the non size-selected NCs towards

259   oxidation-reduction cycle. Surface restructuring[44, 52] of monocrystalline Au surfaces upon Au

260   electro-oxidation and subsequent reduction generally promotes a roughening of smooth bulk

261   electrode surfaces due to the development of monoatomic pits during the oxide reduction.[53]

262   At high applied potentials it may even become destructive if a significant 'turnover process'

263   occurs. [52, 54]

264   Finally, chemically prepared Au colloid electrodes (Figure 3f) did not show any MEO activity

265   peaks (Peak I and II) despite the Au loading being 50 times higher (21 µg cm^{-2}) than that of Au

266   NCs samples. This may be attributed to a significant decrease in the ECSA caused by

267   agglomeration of NPs on the FTO surface (Figure 2b) as well as to the presence of

268   cetyltrimethylammonium bromide (CTAB) surfactant remaining at the Au surface that may

269   both limit the access of the reactants to the active sites and hinder their formation at the Au

270   metal surfaces. The detrimental role of surfactant passivating the surface of Au NPs on their

271 catalytic activity is supported by the absence of MEO activity (Figure S9) on a more dispersed

272 test sample of drop-casted colloidal Au NPs intentionally left unwashed on the FTO surface

273 (SEM image presented in Figure S8).

274 The stability and electrochemical activity of FTO modified with Au NCs and colloidal Au NPs

275 were measured by chronoamperometry. The electrodes were held at a potential of 0.158 V for

276 400 s in stationary electrolytes (0.5 M KOH+ 5 M CH$_3$OH). The temporal evolution of the Au

277 mass normalized current (Figure S10) demonstrates, in both systems, a drop in the initial

278 currents followed by a tendency to approach a limiting value. The relatively longer time taken

279 by Au NCs to reach stable currents reflects the higher stability of Au NCs compared to Au

280 colloids. At 400s, the Au mass normalized currents measured for Au NCs and colloidal Au NPs

281 are 116.5 µA µg^{-1}Au and 0.6 µA µg^{-1}Au, respectively. This high rate further confirms the

282 outstanding catalytic performance and relative stability over this timescale of Au NCs towards

283 methanol oxidation. Compared to the mass activity of chemically prepared nanostructured Au

284 catalysts reported in literature, for example, Au NPs supported on carbon (48.6 mA·mg^{-1}

285 Au),[16] AuNi/C (52.9 mA mg^{-1} Au), [55] and hollow nanoporous gold and solid Au (equivalent

286 to 42.5 mA mg^{-1} Au at 5M MeOH),[56] the Au NCs catalyst presents a 6 to 7 times enhanced

287 activity under identical methanol electro-oxidation conditions.[51] Pairing Au with other

288 elements and/or active supports[57] may improve the mass activity of Au-based NCs further to

289 match that of state-of-the-art Pt/C catalyst that was found 4 times more active under the test

290 conditions used in this work (Figure S11).

291

292 **Origin of nanoclustered gold catalytic activity enhancement**

293 To unravel the origin of the superior electrocatalytic properties of Au NCs, the relationship

294 between their physical characteristics and their MEO activity was further investigated by first-

295 principles calculations. We have computationally synthesized an Au cluster with

296 experimentally known 3 nm size. The geometric structure of the Au cluster obtained using

297   simulated annealing (starting from a Wulff constructed 3 nm particle consisting of 807 atoms)

298   closely resembles that of the deposited catalyst (see Figure S12 and SI methods section for

299   details). Before characterizing the surface Au sites, the simulated Au_{807} structure was refined

300   by the ReaxFF force field method. 100 to 200-atom models centered on the adsorption site

301   within a cut-off distance probed by the OH binding energy on reference Au(111) surface (Figure

302   S13) were extracted from the Au_{807} cluster for further DFT computations. [58] A cut-off distance

303   of 11 Å is selected, large enough to separately describe the on-top and the bridge site with a

304   computational accuracy of 0.06 eV.

305   The computationally synthesized Au_{807} has a quasi-icosahedral shape with an average

306   coordination of 10.4 in excellent agreement with the EXAFS value (illustrated in Figure S14

307   and Table S2). The stability of the simulated Au_{807} quasi-icosahedral structure is in line with

308   previous theoretical simulations,[18, 59] and experimental investigations highlighting the

309   occurrence of various structures for this cluster size [32] (Figure S1).

310   Previous studies have demonstrated that the adsorption free energies of CO (ΔG_{CO}) and OH

311   (ΔG_{OH}) are good descriptors of MEO reaction.[60, 61] Adsorption free energies of all methanol

312   decomposition intermediates binding through carbon or oxygen atoms with various catalytic

313   metal surfaces were shown to scale linearly with ΔG_{CO} or $\Delta G_{OH,}$ respectively. Moreover, the

314   limiting potential for methanol activation following a clear volcano plot with respect to these

315   variables was reported.[60, 61] In line with references[60, 61], we based the adsorption free energies

316   of CO and OH to those of $CO_{2(g)}$ and $H_2O_{(l)}$ respectively at standard conditions, and apply the

317   Computational Hydrogen Electrode (CHE) model,[62] given that the anodic reaction of the

318   complete methanol oxidation is $CH_3OH(g) + H_2O(l) \rightarrow CO_2(g) + 6H^+ + 6e^-$ (see SI methods

319   section for the details). Although the exact values depend slightly on the computational details,

320   the consistent choice of the descriptors makes it possible to compare the computed trends to

321   that in references.[60, 61]

322   This shows that the low methanol oxidation activity of Au(111) surface is due to the highly

323   positive ΔG_{CO} and ΔG_{OH} values and their decrease is desirable to reduce the MEO efficiency.[61]

324   We directly modelled the interaction of CO and OH molecules with a quasi-icosahedral Au_{807}

325   and a reference octahedral Au_{891} cluster (Figure S15 and Table S3). The adsorption energies

326   and adsorption free energies of OH and CO are computed for several possible adsorption sites

327   and further compared with those on an Au(111) extended surface (**Figure 4**).

328   CO and OH adsorption free energies computed at different adsorption sites of the quasi-

329   icosahedron Au_{807} and the octahedron Au_{891} are generally less positive than those obtained on

330   at the Au(111) surface (Figure S15). More specifically we find that the CO and OH adsorption

331   free energies at the vertices of the Au_{807} quasi-icosahedron cluster are even less positive than

332   those on the Au_{891} octahedron cluster with the lowest values close to those of the stepped

333   Au(221) surface exposing under-coordinated atoms.[61] As the ability of under-coordinated Au

334   atoms to bind adsorbates is closely related to the barriers for surface reactions,[19] the edges and

335   especially the vertices of Au clusters are expected to be the most active catalytic sites.

336   In the icosahedral clusters the number of vertex sites is 12, thus the fraction of under-

337   coordinated surface atoms scales with the decreasing cluster size with respectively 2% vertex,

338   21% edge and 21% face atoms for 2.5 nm Au_{561} and 1% vertex, 16% edge and 22% face atoms

339   for 3 nm Au_{807} (Figure S16). Thus, due to a simple geometric scaling the smaller clusters are

340   expected to have larger activity than much larger clusters such as 4.8 nm Au_{3871} that features

341   0.3% vertex, 7 % edge and 19% face atoms. Similarly, the fraction of catalytically inactive core

342   atoms is 56% in Au_{561}, 61% in Au_{807}, and reaches 74% in Au_{3871}. However, the higher surface

343   to volume ratio of the very small clusters in sub nanometer range leads to higher surface energy,

344   thus a decreased stability, what is demonstrated in Figure S17. Thus, the activity of

345   nanoclustered Au is determined by the balance between these two effects and the 2-4 nm size

346   range exhibits a good balance between the relatively high surface site density and the stability.
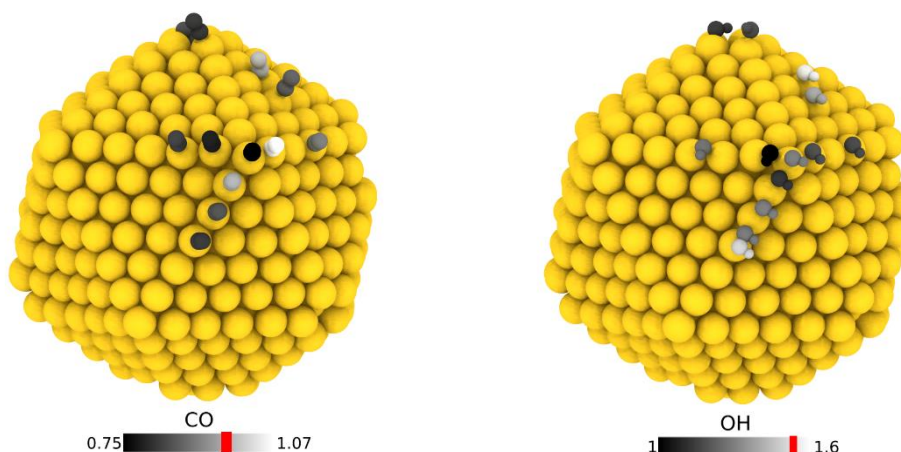
Figure 4: Adsorption sites and the corresponding adsorption free energies of CO and OH⁻ in eV at various sites of the Au_{807} cluster. Each adsorbant represents a separate computation. Reference values, computed for the Au(111) surface, are marked in red on the scale bars.

347 We then attribute the exceptional catalytic performance of size-selected 3nm Au NCs deposited

348 on FTO electrodes to the high density of highly active under-coordinated surface atoms

349 compared to the total number of atoms optimal at this cluster size combined to an improved

350 stability towards oxidation of the cluster's faceted structure. The decrease of the adsorption free

351 energy at neutral potential at the vertex sites of Au_{807} compared to that on Au(111) surface is

352 even more remarkable for OH (0.6 eV from 1 eV at cluster vertices to 1.6 eV at Au(111)

353 surface) than for CO. Similar but weaker effects are also obtained for the cluster edge atoms

354 that separate two facets. Decrease in adsorption free energy of OH is expected to increase the

355 amount of fractional charge transferred (λe-), giving rise to a more polarized Au-OH$_{ads}^{(1-\lambda)-}$

356 surface. As a result, the interaction between Au-OH$_{ads}^{(1-\lambda)-}$ and methanol is expected to

357 strengthen, leading to a high MEO activity.[63] This enhanced interaction of methanol with the

358 under-coordinated sites of Au NCs is unhampered by the water molecules, as the surface charge

359 of Au is negative in the potential region of -150-400 mV.[10]

360 The importance of selecting the optimal Au cluster size is demonstrated by the substantial lower

361 activity of the control electrode produced by depositing non size-selected sub 5 nm Au clusters

362 that is comparable to that reported for other Au NPs.. This is attributed to a lower density of

363 under-coordinated atoms resulting from the important atomic fraction forming the large clusters

364 (4 to 5 nm) as seen on the atom-weighted distribution (Figure S6c). The mixture of cluster sizes

365 ranging from few atom clusters to larger 5 nm structures is also expected to favour a loss of

366 ECSA through Ostwald ripening, agglomeration and/or more severe corrosion of the oligomeric

367 clusters.[8, 64] On the other hand, remarkable stability of size-selected Au NCs faceted structures

368 versus non size-selected NCs upon oxidation-reduction at 20 mVs^{-1} scan rate is highlighted, as

369 discussed above, both by the absence of hysteresis above 400 mV and of a electrochemical

370 reduction peak in the backward scan. The absence of activity of chemical Au colloids is likely

371 the consequence of the presence of ligands, which are (1) hindering the crystallization of a

372 faceted Au structure (2) preventing access for the reactants to the Au surface sites. This clearly

373 demonstrates the benefit of using CBD technology over chemical preparations. Ligand removal

374 by high temperature annealing that favours their sintering is likely inadequate to reproduce the

375 highly symmetrical crystal structures of deposited Au clusters.

376 The production of this novel highly active Au electrocatalyst for MEO has been made possible

377 by the gas-phase CBD technology that allows a precise selection of cluster sizes not always

378 accessible by conventional chemistry yielding a majority of low energy highly ordered

379 structures featuring a large fraction of vertices and edges surface atoms. Moreover the

380 crystallization of the Au NCs structures likely occurs more easily in the gas phase where Au

381 clusters are free from any gas or support interaction.[65] The dispersion of these naked clusters

382 is preserved upon soft landing on the FTO surface. The high stability of these (quasi)crystalline

383 structures make them resistant to oxidation during the CV scans avoiding their deactivation by

384 surface restructuring.

385

386 **Conclusion**

387 In this work, we have used the CBD approach to design a novel MEO catalyst based on highly

388 dispersed 3 nm zero valence deposited Au clusters that exhibit exceptional mass and specific

389 activity of 329 µA µg^{-1} Au and 2 mA cm^{-2} respectively, at MEO potential of 160 mV (vs SCE

390 at 20 mV s^{-1}). The enhanced activity of nanoclustered Au is tied by DFT to the high density of

391 highly active under-coordinated edge and vertex surface Au atoms resulting from the faceted

392 geometries of the Au clusters deposited on FTO by CBD. These Au atoms strongly bind CO

393 and OH enhancing the interaction with methanol, while high dispersion and stability of the

394 cluster (quasi)crystalline structure prevents their destructive oxidation. We anticipate that this

395 work further motivates the rational design of high performance Au based electrocatalysts that

396 could replace Pt as fuel cell catalyst.

397

398

399 **Supporting Information**
400
401 Supporting Information is available from the Wiley Online Library or from the authors.
402
403
404

417   contributed equally to this manuscript. A.Y. and T.W.L. prepared the CBD samples. Y.L.

418   synthesized the colloidal Au samples and performed the electrochemical study. K.J.H. and A.Y.

419   performed STEM measurements. O.V.S, D.G., A.Y., and T.W.L performed the XAFS

420   measurement. J.E.S. performed SEM imaging. T.H. performed the DFT calculations. P.L. and

421   E.J. managed the study. A.Y. and D.G. coordinated the writing of the paper with contributions

422   of all co-authors.

423

427

428

429

430

References

[1] P. Joghee, J. N. Malik, S. Pylypenko, R. O'Hayre, MRS Energy & Sustainability 2015, 2, E3.

[2] G. A. Olah, A. Goeppert, G. K. S. Prakash, *Beyond Oil and Gas: The Methanol Economy*, 2011; G. A. Olah, A. Goeppert, G. K. S. Prakash, The Journal of Organic Chemistry 2009, 74, 487.

[3] A. Kongkanand, M. F. Mathias, The Journal of Physical Chemistry Letters 2016, 7, 1127; A. Ganesan, M. Narayanasamy, Materials for Renewable and Sustainable Energy 2019, 8, 18; L. Chong, J. Wen, J. Kubal, F. G. Sen, J. Zou, J. Greeley, M. Chan, H. Barkholtz, W. Ding, D.-J. Liu, Science 2018, 362, 1276.

[4] F. Jing, R. Sun, S. Wang, H. Sun, G. Sun, Energy & Fuels 2020, 34, 3850; S. D. Knights, K. M. Colbow, J. St-Pierre, D. P. Wilkinson, Journal of Power Sources 2004, 127, 127.

[5] Y. Tong, X. Yan, J. Liang, S. X. Dou, Small 2019, n/a, 1904126; Q. Sun, H. Xu, Y. Du, ChemSusChem 2020, 13, 2540.

[6] W. Huang, H. Wang, J. Zhou, J. Wang, P. N. Duchesne, D. Muir, P. Zhang, N. Han, F. Zhao, M. Zeng, J. Zhong, C. Jin, Y. Li, S.-T. Lee, H. Dai, Nature Communications 2015, 6, 10035; J. S. Spendelow, A. Wieckowski, Physical Chemistry Chemical Physics 2007, 9, 2654.

[7] L. Xing, G. Jerkiewicz, D. Beauchemin, Analytica Chimica Acta 2013, 785, 16; S. Cherevko, N. Kulyk, K. J. J. Mayrhofer, Nano Energy 2016, 29, 275.

[8] R. Borup, J. Meyers, B. Pivovar, Y. S. Kim, R. Mukundan, N. Garland, D. Myers, M. Wilson, F. Garzon, D. Wood, P. Zelenay, K. More, K. Stroh, T. Zawodzinski, J. Boncella, J. E. McGrath, M. Inaba, K. Miyatake, M. Hori, K. Ota, Z. Ogumi, S. Miyata, A. Nishikata, Z. Siroma, Y. Uchimoto, K. Yasuda, K.-i. Kimijima, N. Iwashita, Chemical Reviews 2007, 107, 3904.

[9] P. Rodriguez, M. T. M. Koper, Phys Chem Chem Phys 2014, 16, 13583; S. Cosentino, G. Fiaschi, V. Strano, K.-j. Hu, T.-W. Liao, N. M. Hemed, A. Yadav, S. Mirabella, D. Grandjean, P. Lievens, Y. Shacham-Diamand, The Journal of Physical Chemistry C 2017, 121, 15644; B. Liu, H. Yao, W. Song, L. Jin, I. M. Mosa, J. F. Rusling, S. L. Suib, J. He, J Am Chem Soc 2016, 138, 4718; S. Pedireddy, H. K. Lee, W. W. Tjiu, I. Y. Phang, H. R. Tan, S. Q. Chua, C. Troadec, X. Y. Ling, Nat Commun 2014, 5, 4947; H. Xia, Y. Ran, H. Li, X. Tao, D. Wang, J Mater Chem A 2013, 1, 4678; Y. Qin, Y. Song, N. Sun, N. Zhao, M. Li, L. Qi, Chem Mater 2008, 20, 3965; Y. Song, T. Miao, P. Zhang, C. Bi, H. Xia, D. Wang, X. Tao, Nanoscale 2015, 7, 8405.

[10] J. Hernández, J. Solla-Gullón, E. Herrero, A. Aldaz, J. M. Feliu, Electrochimica Acta 2006, 52, 1662.

[11] J. Zhang, P. Liu, H. Ma, Y. Ding, The Journal of Physical Chemistry C 2007, 111, 10382.

[12] G. Tremiliosi-Filho, E. R. Gonzalez, A. J. Motheo, E. M. Belgsir, J. M. Léger, C. Lamy, J Electroanal Chem 1998, 444, 31.

[13] Z. Wang, J. Du, Y. Zhang, J. Han, S. Huang, A. Hirata, M. Chen, Nano Energy 2019, 56, 286.

[14] K. A. Assiongbon, D. Roy, Surface Science 2005, 594, 99.

[15] P. Santhosh, A. Gopalan, K.-P. Lee, J Catal 2006, 238, 177.

[16] S. Yan, S. Zhang, Y. Lin, G. Liu, The Journal of Physical Chemistry C 2011, 115, 6986.

[17] W. Zhu, R. Michalsky, Ö. Metin, H. Lv, S. Guo, C. J. Wright, X. Sun, A. A. Peterson, S. Sun, J Am Chem Soc 2013, 135, 16833.

[18] S. Back, M. S. Yeom, Y. Jung, Acs Catal 2015, 5, 5089.

[19] N. Lopez, T. V. W. Janssens, B. S. Clausen, Y. Xu, M. Mavrikakis, T. Bligaard, J. K. Nørskov, Journal of Catalysis 2004, 223, 232.

481 [20] M. Haruta, Nature 2005, 437, 1098; H. Tsunoyama, H. Sakurai, Y. Negishi, T. Tsukuda,
482   J Am Chem Soc 2005, 127, 9374; M. Haruta, Catal Today 1997, 36, 153; A. S. K. Hashmi,
483   G. J. Hutchings, Angew Chem Int Edit 2006, 45, 7896; S. Ye, A. P. Brown, A. C.
484   Stammers, N. H. Thomson, J. Wen, L. Roach, R. J. Bushby, P. L. Coletta, K. Critchley,
485   S. D. Connell, A. F. Markham, R. Brydson, S. D. Evans, Advanced Science 2019, 6,
486   1900911; J. J. Gooding, Chemistry – A European Journal 2019, 25, 5335; R. Ciriminna,
487   E. Falletta, C. Della Pina, J. H. Teles, M. Pagliaro, Angewandte Chemie International
488   Edition 2016, 55, 14210; G. Malta, S. A. Kondrat, S. J. Freakley, C. J. Davies, L. Lu, S.
489   Dawson, A. Thetford, E. K. Gibson, D. J. Morgan, W. Jones, P. P. Wells, P. Johnston, C.
490   R. A. Catlow, C. J. Kiely, G. J. Hutchings, Science 2017, 355, 1399.
491 [21] M. Comotti, C. Della Pina, R. Matarrese, M. Rossi, Angewandte Chemie International
492   Edition 2004, 43, 5812.
493 [22] M. Valden, X. Lai, D. W. Goodman, Science 1998, 281, 1647; M. Valden, S. Pak, X. Lai,
494   D. W. Goodman, Catal Lett 1998, 56, 7; G. R. Bamwenda, S. Tsubota, T. Nakamura, M.
495   Haruta, Catal Lett 1997, 44, 83; M. Haruta, Physics and Chemistry of Clusters 2001, 117,
496   99.
497 [23] S. Guerin, B. E. Hayden, D. Pletcher, M. E. Rendall, J.-P. Suchsland, Journal of
498   Combinatorial Chemistry 2006, 8, 679.
499 [24] W. Tang, H. Lin, A. Kleiman-Shwarsctein, G. D. Stucky, E. W. McFarland, The Journal
500   of Physical Chemistry C 2008, 112, 10515.
501 [25] Y. Xu, M. Mavrikakis, The Journal of Physical Chemistry B 2003, 107, 9298; N. Lopez,
502   J. K. Nørskov, J Am Chem Soc 2002, 124, 11262.
503 [26] G. C. Bond, Molecules 2012, 17, 1716.
504 [27] N. Saliba, D. H. Parker, B. E. Koel, Surf Sci 1998, 410, 270.
505 [28] A. R. Poerwoprajitno, L. Gloag, S. Cheong, J. J. Gooding, R. D. Tilley, Nanoscale 2019,
506   11, 18995.
507 [29] M. Okumura, T. Akita, M. Haruta, Catal Today 2002, 74, 265; H. Li, Z. Li, Y. Yu, Y.
508   Ma, W. Yang, F. Wang, X. Yin, X. Wang, The Journal of Physical Chemistry C 2017,
509   121, 12071.
510 [30] C. Zeng, Y. Chen, K. Kirschbaum, K. J. Lambright, R. Jin, Science 2016, 354, 1580.
511 [31] Z. Li, H.-Y. T. Chen, K. Schouteden, T. Picot, T.-W. Liao, A. Seliverstov, C. Van
512   Haesendonck, G. Pacchioni, E. Janssens, P. Lievens, Science Advances 2020, 6,
513   eaay4289; T.-W. Liao, A. Yadav, P. Ferrari, Y. Niu, X.-K. Wei, J. Vernieres, K.-J. Hu,
514   M. Heggen, R. E. Dunin-Borkowski, R. E. Palmer, K. Laasonen, D. Grandjean, E.
515   Janssens, P. Lievens, Chemistry of Materials 2019, 31, 10040; T. W. Liao, A. Yadav, K.
516   J. Hu, J. van der Tol, S. Cosentino, F. D'Acapito, R. E. Palmer, C. Lenardi, R. Ferrando,
517   D. Grandjean, P. Lievens, Nanoscale 2018, 10, 6684; A. Yadav, R. Pandey, T.-W. Liao,
518   V. S. Zharinov, K.-J. Hu, J. Vernieres, R. E. Palmer, P. Lievens, D. Grandjean, Y.
519   Shacham-Diamand, Nanoscale 2020, 12, 6047.
520 [32] S. R. Plant, L. Cao, R. E. Palmer, J Am Chem Soc 2014, 136, 7559.
521 [33] Z. W. Wang, R. E. Palmer, Nanoscale 2012, 4, 4947.
522 [34] Z. W. Wang, R. E. Palmer, Nano Lett 2012, 12, 5510.
523 [35] Z. Y. Li, N. P. Young, M. Di Vece, S. Palomba, R. E. Palmer, A. L. Bleloch, B. C. Curley,
524   R. L. Johnston, J. Jiang, J. Yuan, Nature 2008, 451, 46.
525 [36] Z. W. Wang, R. E. Palmer, Phys Rev Lett 2012, 108.
526 [37] Y. Negishi, Y. Takasugi, S. Sato, H. Yao, K. Kimura, T. Tsukuda, Journal of the
527   American Chemical Society 2004, 126, 6518; T. Higaki, Y. Li, S. Zhao, Q. Li, S. Li, X.-
528   S. Du, S. Yang, J. Chai, R. Jin, Angewandte Chemie International Edition 2019, 58, 8291;
529   X. Du, R. Jin, ACS Nano 2019, 13, 7383.
530 [38] T.-W. Liao, A. Yadav, K.-J. Hu, J. van der Tol, S. Cosentino, F. D'Acapito, R. E. Palmer,
531   C. Lenardi, R. Ferrando, D. Grandjean, P. Lievens, Nanoscale 2018, 10, 6684.

532 [39] M. Giorgetti, G. Aquilanti, B. Ballarin, M. Berrettoni, M. C. Cassani, S. Fazzini, D. Nanni,
533 D. Tonelli, Analytical Chemistry 2016, 88, 6873; S.-Y. Chang, A. Uehara, S. G. Booth,
534 K. Ignatyev, J. F. W. Mosselmans, R. A. W. Dryfe, S. L. M. Schroeder, RSC Advances
535 2015, 5, 6912.
536 [40] R. E. Benfield, Journal of the Chemical Society, Faraday Transactions 1992, 88, 1107; N.
537 S. Marinković, K. Sasaki, R. R. Adžić, Zaštita materijala 2016, 57, 101.
538 [41] J. T. Miller, A. J. Kropf, Y. Zha, J. R. Regalbuto, L. Delannoy, C. Louis, E. Bus, J. A.
539 van Bokhoven, J Catal 2006, 240, 222; R. E. Benfield, D. Grandjean, M. Kröll, R. Pugin,
540 T. Sawitowski, G. Schmid, The Journal of Physical Chemistry B 2001, 105, 1961.
541 [42] A. Chen, J. Lipkowski, The Journal of Physical Chemistry B 1999, 103, 682.
542 [43] J. Luo, P. N. Njoki, Y. Lin, D. Mott, L. Y. Wang, C. J. Zhong, Langmuir 2006, 22, 2892;
543 A. Kowal, M. Li, M. Shao, K. Sasaki, M. B. Vukmirovic, J. Zhang, N. S. Marinkovic, P.
544 Liu, A. I. Frenkel, R. R. Adzic, Nat Mater 2009, 8, 325.
545 [44] A. Hamelin, J Electroanal Chem 1996, 407, 1.
546 [45] Z. Borkowska, A. Tymosiak-Zielinska, G. Shul, Electrochim Acta 2004, 49, 1209; M.
547 Avramov-Ivić, V. Jovanović, G. Vlajnić, J. Popić, J Electroanal Chem 1997, 423, 119.
548 [46] B. Ni, P. He, W. Liao, S. Chen, L. Gu, Y. Gong, K. Wang, J. Zhuang, L. Song, G. Zhou,
549 X. Wang, Small 2018, 14, 1703749.
550 [47] M. Graf, M. Haensch, J. Carstens, G. Wittstock, J. Weissmüller, Nanoscale 2017, 9,
551 17839.
552 [48] Z. Borkowska, A. Tymosiak-Zielinska, R. Nowakowski, Electrochim Acta 2004, 49,
553 2613.
554 [49] W. Ye, H. Kou, Q. Liu, J. Yan, F. Zhou, C. Wang, International Journal of Hydrogen
555 Energy 2012, 37, 4088.
556 [50] L. Y. Chen, T. Fujita, Y. Ding, M. W. Chen, Advanced Functional Materials 2010, 20,
557 2279; X.-J. Huang, D. S. Silvester, I. Streeter, L. Aldous, C. Hardacre, R. G. Compton,
558 The Journal of Physical Chemistry C 2008, 112, 19477.
559 [51] Z. Mao, H. Hu, R. Su, P. Liu, Y. Li, W. Zhang, X. Zhao, J. Guo, P. Guan, G. Qin, X.
560 Zhang, ChemCatChem 2018, 10, 141.
561 [52] M. A. Schneeweiss, D. M. Kolb, Solid State Ionics 1997, 94, 171.
562 [53] R. J. Nichols, O. M. Magnussen, J. Hotlos, T. Twomey, R. J. Behm, D. M. Kolb, Journal
563 of Electroanalytical Chemistry and Interfacial Electrochemistry 1990, 290, 21.
564 [54] W. Polewska, C. M. Vitus, B. M. Ocko, R. R. Adzic, J Electroanal Chem 1994, 364, 265.
565 [55] S. Yan, L. Gao, S. Zhang, L. Gao, W. Zhang, Y. Li, International Journal of Hydrogen
566 Energy 2013, 38, 12838.
567 [56] S. Pedireddy, H. K. Lee, W. W. Tjiu, I. Y. Phang, H. R. Tan, S. Q. Chua, C. Troadec, X.
568 Y. Ling, Nat Commun 2014, 5, 4947.
569 [57] S. Lu, H. Li, J. Sun, Z. Zhuang, Nano Research 2018, 11, 2058; D. Strmcnik, M.
570 Uchimura, C. Wang, R. Subbaraman, N. Danilovic, D. van der Vliet, A. P. Paulikas, V.
571 R. Stamenkovic, N. M. Markovic, Nature Chemistry 2013, 5, 300; R. Subbaraman, D.
572 Tripkovic, K.-C. Chang, D. Strmcnik, A. P. Paulikas, P. Hirunsit, M. Chan, J. Greeley,
573 V. Stamenkovic, N. M. Markovic, Nature Materials 2012, 11, 550; Y. Shen, Z. Zhang, R.
574 Long, K. Xiao, J. Xi, ACS Applied Materials & Interfaces 2014, 6, 15162; T. Liu, C. Li,
575 Q. Yuan, ACS Omega 2018, 3, 8724.
576 [58] T. Cheng, Y. Huang, H. Xiao, W. A. Goddard, The Journal of Physical Chemistry Letters
577 2017, 8, 3317; Y. Chen, Y. Huang, T. Cheng, W. A. Goddard, Journal of the American
578 Chemical Society 2019, 141, 11651.
579 [59] Y. Wang, S. Teitel, C. Dellago, The Journal of Chemical Physics 2005, 122, 214722.
580 [60] P. Ferrin, A. U. Nilekar, J. Greeley, M. Mavrikakis, J. Rossmeisl, Surface Science 2008,
581 602, 3424.
582 [61] G. A. Tritsaris, J. Rossmeisl, The Journal of Physical Chemistry C 2012, 116, 11980.

583   [62] J. K. Nørskov, J. Rossmeisl, A. Logadottir, L. Lindqvist, J. R. Kitchin, T. Bligaard, H.
584   Jónsson, The Journal of Physical Chemistry B 2004, 108, 17886.
585   [63] E. Gonzalez Hernan, C. Alonso, J. Gonzalez-Velasco, Journal of Applied
586   Electrochemistry 1987, 17, 868.
587   [64] A. Howard, C. E. J. Mitchell, R. G. Egdell, Surf Sci 2002, 515, L504; M. Di Vece, D.
588   Grandjean, M. J. Van Bael, C. P. Romero, X. Wang, S. Decoster, A. Vantomme, P.
589   Lievens, Phys Rev Lett 2008, 100; M. Wanner, R. Werner, D. Gerthsen, Surf Sci 2006,
590   600, 632.
591   [65] F. Baletto, Journal of Physics: Condensed Matter 2019, 31, 113001.
592

593

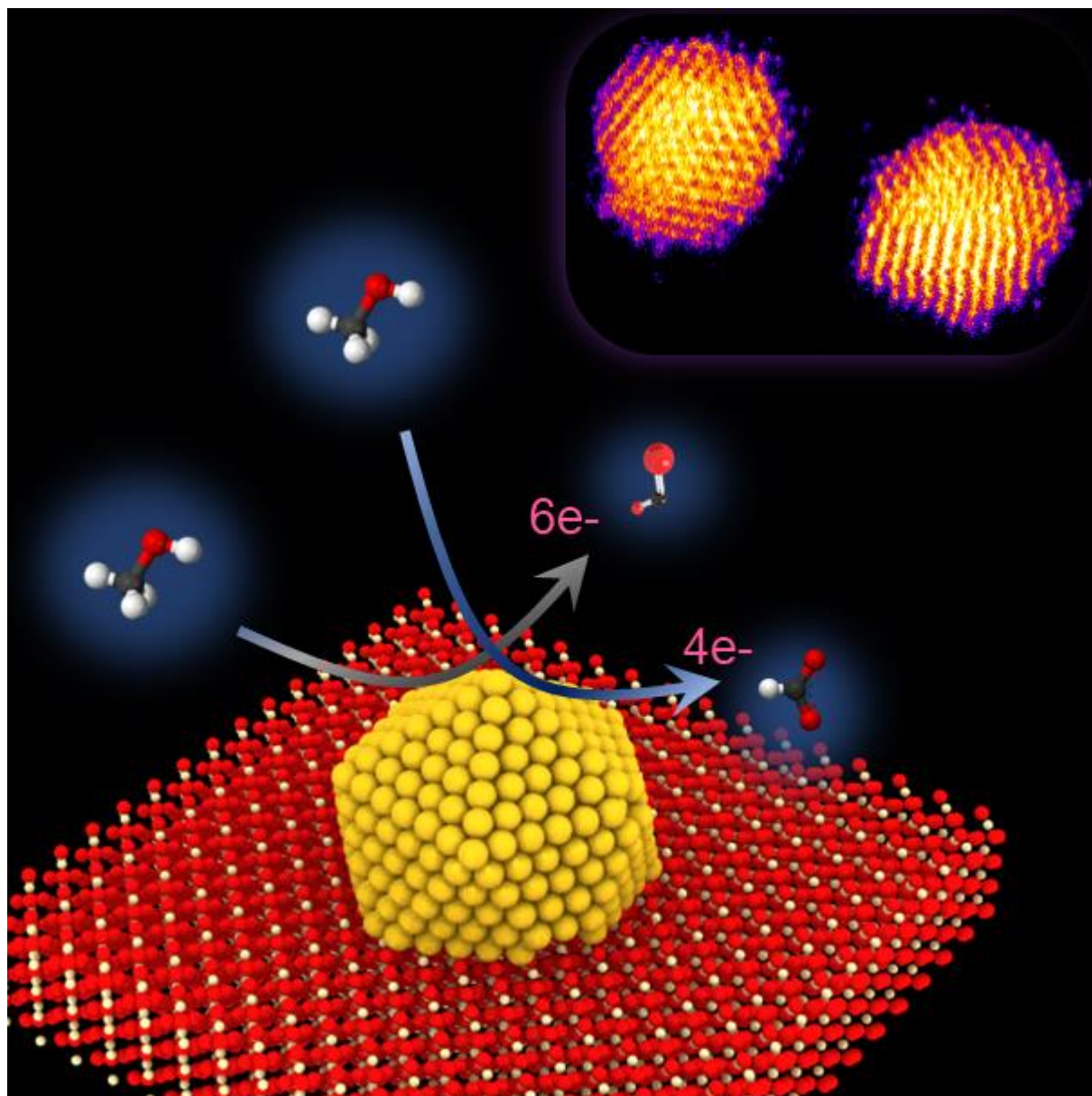**Abstract Graphics**

595
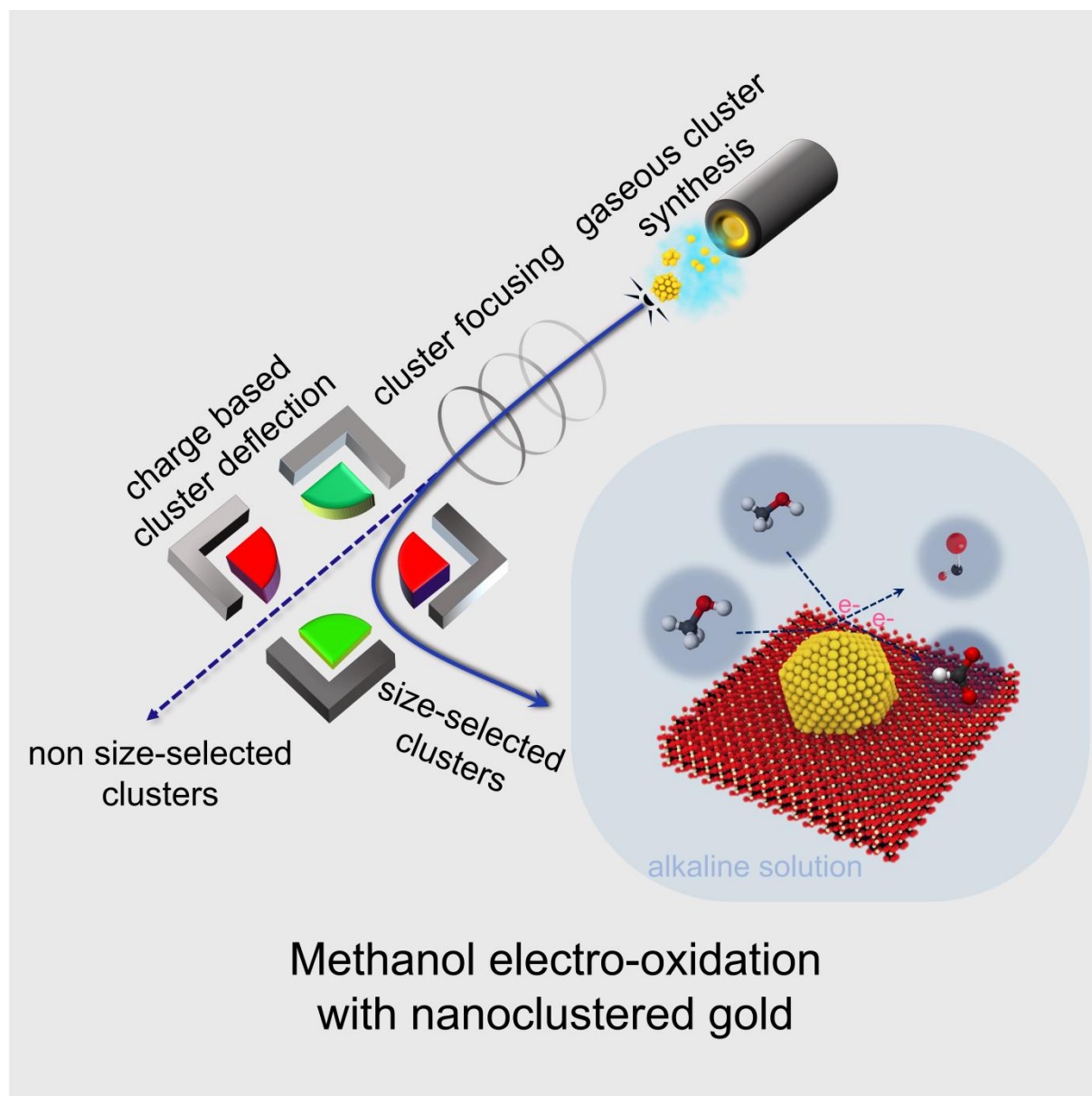
596

597

598

599 **Cover Art**

600 **Enhanced methanol electro oxidation by nanoclustered gold**

601

602